Research Article

Junfei Tong#, Pengfei Dong#, Sachin Kedar, Deepta Ghate, and Linxia Gu*

Three-dimensional shape analysis of peripapillary retinal pigment epithelium-basement membrane layer based on OCT radial images

https://doi.org/10.1515/ntrev-2021-0035
received May 12, 2021; accepted May 27, 2021

Abstract: The peripapillary retinal pigment epithelium-basement membrane (ppRPE/BM) layer angle was recently proposed as a potential index for estimating intracranial pressure noninvasively. However, the ppRPE/BM layer angle, measured from the optical coherence tomography (OCT) scans, varied across the radial directions of the optic disc. This made the ppRPE/BM layer angle difficult to be utilized in its full potential. In this study, we developed a mathematical model to quantify the ppRPE/BM layer angles across radial scans in relation to the ppRPE/BM 3D morphology in terms of its 3D angle and scanning tilt angles. Results showed that the variations of the ppRPE/BM layer angle across radial scans were well explained by its 3D angle and scanning tilt angles. The ppRPE/BM layer 3D angle was reversely fitted from the measured ppRPE/BM layer angles across radial directions with application to six eyes from four patients, who underwent medically necessary lumbar puncture. The fitted curve from our mathematical model matched well with the experimental measurements ($R^2 > 0.9$ in most cases). This further validated our mathematical model. The proposed model in this study has elucidated the variations of ppRPE/BM layer angle across 2D radial scans from the perspective of the ppRPE/BM layer 3D morphology. It is expected that the ppRPE/BM layer 3D angle developed in this study could be further exploited as a new biomarker for the optic disc.

Keywords: optical coherence tomography, retinal layer, tilt, ppRPE/BM layer angle, mathematical model, imaging analysis, intracranial pressure

1 Introduction

Optical coherence tomography (OCT) has been widely used in ophthalmology for providing high-resolution *in vivo* retinal structures [1,2]. The retinal OCT scans have been used for the diagnosis and the assessment of various ophthalmological diseases (*e.g.*, glaucoma and macular edema) [3–5]. In our recent study, we found that the angle of the peripapillary retinal pigment epithelium-basement membrane (ppRPE/BM) layer changed following the reduced intracranial pressure (ICP) procedure [6]. This implies that the ppRPE/BM layer angle might be a potential index for the noninvasive assessment of the ICP, which is of great importance in clinical practice as abnormal ICP is a major risk factor for ophthalmological and neurological diseases [7–10]. Such noninvasive ICP assessment would also be highly valuable to human health countermeasures for spaceflight to mitigate microgravity-induced visual impairments [11,12].

Common OCT images consisted of multiple B-scans, each of which provides a two-dimensional (2D) cross-

# Junfei Tong and Pengfei Dong contributed equally to this work.

*** Corresponding author: Linxia Gu,** Department of Biomedical and Chemical Engineering and Sciences, Florida Institute of Technology (FIT), Melbourne, FL 32901, United States of America, e-mail: gul@fit.edu, tel: +1-321-674-8447
Junfei Tong: Department of Mechanical and Materials Engineering, University of Nebraska-Lincoln, Lincoln, NE 68588-0656, United States of America
Pengfei Dong: Department of Biomedical and Chemical Engineering and Sciences, Florida Institute of Technology (FIT), Melbourne, FL 32901, United States of America
Sachin Kedar: Department of Neurological Sciences, University of Nebraska Medical Center, Omaha, NE 68198-8440, United States of America; Stanley Truhlsen Eye Institute, University of Nebraska Medical Center, Omaha, NE 68105-1119, United States of America
Deepta Ghate: Department of Ophthalmology and Visual Sciences, University of Nebraska Medical Center, Omaha, NE 68105-1119, United States of America

sectional view. However, the ppRPE/BM layer angle varied in these 2D scans due to image tilting. Sibony *et al.* [13] have shown that such image tilting was due to the oblique orientation of the scanning beam to the optic disc. Symmetric and untilted OCT scans at the nasal-temporal direction required the scanning beam of the OCT machine to be perpendicular to the optic disc, *e.g.*, parallel to the axis of the optic nerve [13,14]. In this way, the ppRPE/BM layer angle in each radial scan is approximately the same, indicating that the 3D shape of the ppRPE/BM layer is conical. However, such imaging protocol is challenging to be implemented considering the uncontrollable eye movements and operator factors during the acquisition process [15]. In clinical practice, the OCT scanning beam is oblique toward the optic disc, leading to a tilted retinal image [15–18]. Specifically, Hariri *et al.* [15] reported that the mean inclination angle for the macular scans is 14.52 ± 2.63° at temporal positioning. Hong *et al.* [16] reported a mean value of 12.62 ± 5.17° for the scanned angle of the optic nerve head images. Consequently, the acquired retinal images were found tilted differently across the radial directions [6,19], which makes it difficult to determine the ppRPE/BM layer angle of a 3D optic disc based on either a single or multiple radial OCT scans. Furthermore, the image tilt led to the measurement bias in the anatomical study such as thickness and angles [15,16,20–22]. The measurement bias of retinal thickness caused by such image tilt can go up to several dozens of microns, which accounts for >10% of its true thickness. This will also compromise the measurement reproducibility of the retinal thickness [23], which adversely affected the early diagnosis of optic diseases [24]. Therefore, it would be of great importance to comprehensively understand the tilt effect in the OCT scans to provide solutions to mitigate or even eliminate such effects.

In this study, we will delineate why the measured ppRPE/BM layer angle varies across the radial OCT scans from the perspective of its 3D morphology. We also proposed a mathematical model to quantify the relationship between the ppRPE/BM layer 3D morphology (in terms of its 3D angle and scanning tilt angles) and its 2D cross-sectional radial OCT scans (in terms of the ppRPE/BM layer angles). The ppRPE/BM layer 3D angle could be reversely determined from the measured ppRPE/BM layer angles across radial directions. The impact of each factor (*e.g.*, ppRPE/BM layer 3D angle and scanning tilt angles) on the measured ppRPE/BM layer angle in 2D OCT radial scans was further characterized. To the best of our knowledge, this is the first study to unveil the ppRPE/BM layer angle variation across radial directions through mathematical modeling. Furthermore, the imaging data of six eyes from four patients, who underwent medically necessary lumbar puncture, were analyzed using the method herein.

2 Methods

2.1 Schematic diagrams of the 3D ppRPE/BM layer and its 2D radial scans

The image tilting contributes to the variation of the measured ppRPE/BM layer angle across different radial scans, which limits its application in broader fields. It is important to notice the direction and location of the OCT scanning beam is manually controlled by physicians during the image acquisition process, as illustrated in Figure 1 [25]. If the scanning beam can be positioned perpendicular to the optic disc or aligned with the optic nerve, the ppRPE/BM layer angle in each radial scan will be approximately the same [13,14]. In addition, the ppRPE/BM layer was nearly a straight line in the 2D cross-sectional view. These observations implied that the 3D shape of the ppRPE/BM layer is conical in the region of the optic nerve head.

A schematic diagram of the conical ppRPE/BM layer was developed to illustrate variations in the ppRPE/BM layer angles in four imaging scenarios (Figure 2). The 3D ppRPE/BM layer is a portion of the conical surface intersecting with the cylindrical optic nerve and sharing the same axis of symmetry. The ppRPE/BM layer 3D angle (denoted as γ, also referred to as 3D angle) was adopted in this study to be consistent with the ppRPE/BM layer angle (denoted as γ') commonly used in the 2D OCT radial scans [6].

As the axis of the scanning beam coincides with the axis of the optic nerve (Figure 2a), the acquired ppRPE/BM

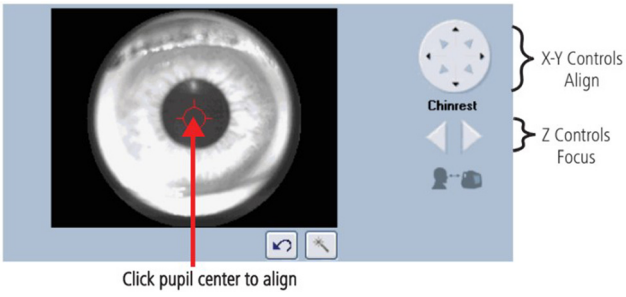

Figure 1: Position control of the OCT scanning beam for the Cirrus HD-OCT machine (Carl Zeiss Meditec, Inc., Dublin, CA). The *X–Y* panel controls the horizontal and vertical movement of the screening center (red circle). The *Z* panel controls the focus.

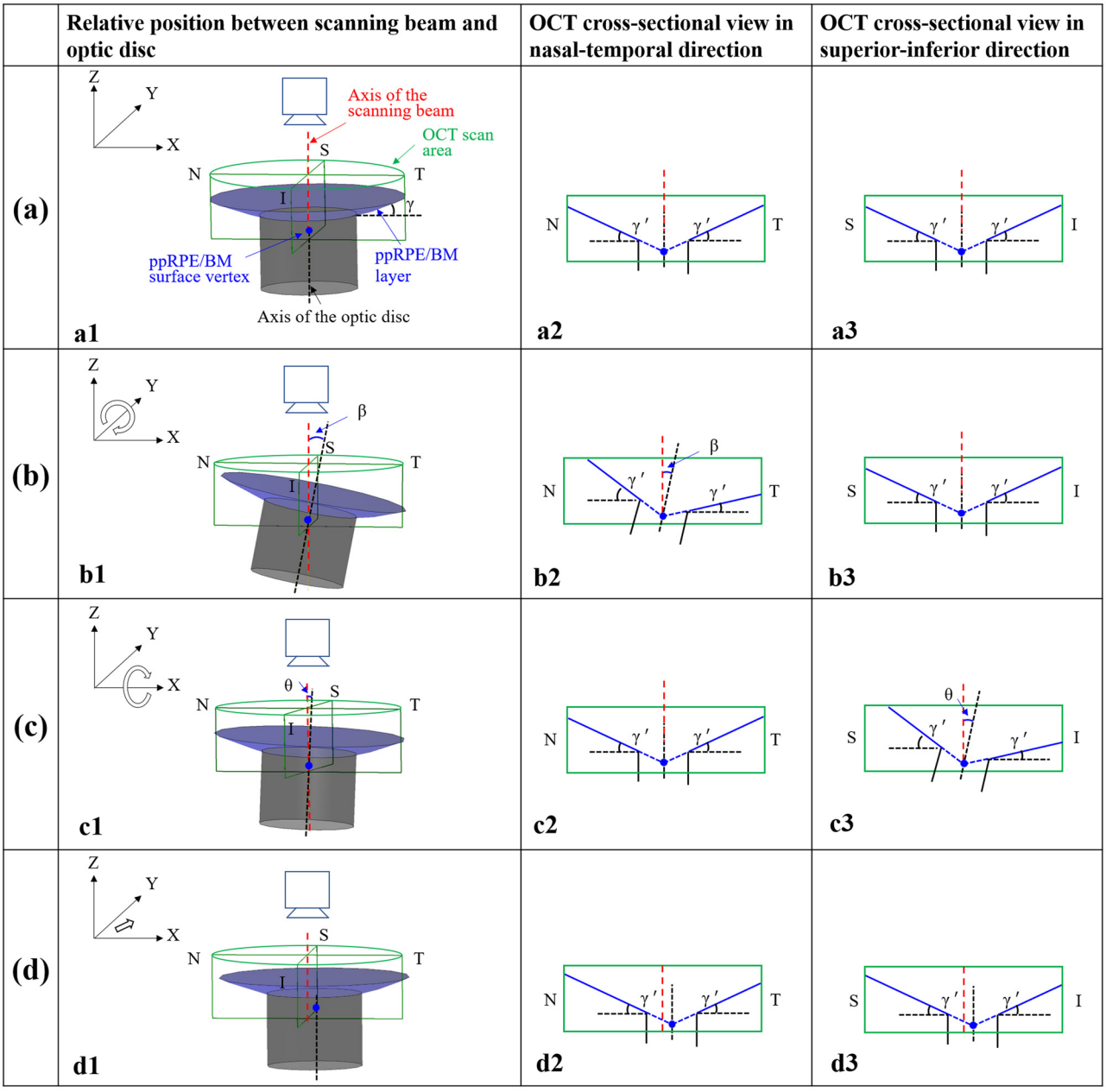

Figure 2: Schematic diagrams of the ppRPE/BM layer morphology with columns: relative position between the OCT scanning beam and optic disc; the OCT cross-sectional view in nasal-temporal direction; and the OCT cross-sectional view in the superior-inferior direction. The ppRPE/BM layer angle (γ') refers to the angle between the ppRPE/BM layer and the horizontal plane of a 2D scan. (Row a) the axis of OCT scanning beam coincides with the axis of the optic disc; (Row b) case with a tilt angle (β) between the axis of OCT scanning beam and the axis of the optic disc in the nasal-temporal direction; (Row c): case with a tilt angle (θ) between the axis of OCT scanning beam and the axis of the optic disc in the superior-inferior direction; (Row d) the axis of OCT scanning beam is parallel with the axis of the optic disc, with the ppRPE/BM surface vertex off the axis of the scanning beam. S, I, N, and T indicate superior, inferior, nasal, and temporal, respectively. The green box marks the OCT scanning area; the blue surface represents the ppRPE/BM layer; the gray surface represents the optic nerve surface. The red dash line represents the axis of the scanning beam, and the black dash line represents the axis of the optic disc. The blue line represents the ppRPE/BM layer in the 2D view, with the blue dashed line as the extended ppRPE/BM layer. The blue dot represents the conical vertex of the ppRPE/BM surface.

layer morphology would be the same across all radial directions (Figure 2a2 and a3). Thus, the measured ppRPE/BM layer angle (γ') would also be the same across the radial directions, which is equal to the ppRPE/BM layer 3D angle (γ). When the axis of the scanning beam has a tilt angle (β) with the axis of the optic disc in the

nasal-temporal direction (Figure 2b), the ppRPE/BM layer would be symmetric in the superior-inferior direction, while it would be tilted in all other directions with the peak tilt occurring in the nasal-temporal direction (Figure 2b2 and b3). When the axis of the scanning beam has a tilt angle (θ) with the axis of the optic disc in the superior-inferior direction (Figure 2c), the ppRPE/BM layer would be symmetric in the nasal-temporal direction, while it would be tilted in all other directions with the peak tilt occurring in the superior-inferior direction (Figure 2c2 and c3). When the axis of the OCT scanning beam is parallel with the axis of the optic disc, with the ppRPE/BM surface vertex of the axis of the scanning beam (Figure 2d), the ppRPE/BM layer angle will still be the same across the radial directions. However, the intersections of the extended ppRPE/BM layer in each scan would have an eccentric distance to the mid-line of each scan (axis of the scanning beam), as shown in Figure 2d2 and d3.

2.2 Experimental data processing

Three right eyes and three left eyes from four patients, who underwent medically necessary lumbar puncture, were analyzed in this study. The details of experimental procedures were introduced in our previous study [6]. Briefly, for each optic disc, 12 uniformly distributed radial OCT scans (an angle of 15° between neighboring scans), illustrated in Figure 3, were acquired using Cirrus HD-OCT (Carl Zeiss Meditec Inc, USA). Each OCT scan had an anatomical size of 1,876 × 625 pixels (6 × 2 mm). Because of the discontinuity and curvature of the ppRPE/BM layer in the central region of the optic disc (highlighted with a red circle in Figure 3a), we quantified the ppRPE/BM layer in the peripheral region between the radius of 1.56 mm (the red circle) and 3 mm (the green circle in Figure 3a). In each OCT radial scan, the ppRPE/BM layer angle to the horizontal plane (Figure 3b and c) was quantified using the semi-automatic method as described in our previous study [6,26]. Here, we organized the calculated ppRPE/BM layer angle based on their radial position from 0° to 345° (denoted as α). We calculated the eccentric distance (denoted as ε) of the intersection point of the two ppRPE/BM layers to the axis of the scanning beam in each scan (Supplement Material). The eccentricity is positive when the intersection point was closer to the temporal side (*e.g.*, Figure 3b).

2.3 Mathematical model of a conical ppRPE/BM layer

A Cartesian coordinate system was established with its Z-axis coinciding with the axis of the OCT scanning beam, as shown in Figure 2a. The conical vertex of the ppRPE/BM surface is set to be in the global X–Y plane. The scanning tilt angle was defined as the angle between the axis of the scanning beam and the axis of the optic disc. The conical ppRPE/BM surface, without tilt angles and vertex translation (*e.g.*, Figure 2a1), could be described by

$$\begin{cases} x = r * \cos(\alpha) \\ y = r * \sin(\alpha) \\ z = r * \tan(\gamma), \end{cases} \tag{1}$$

where r is the distance from any point on the conical surface to the axis of the conical surface, α is the azimuthal angle, and γ is the 3D angle of the ppRPE/BM layer.

Considering a tilt angle (β) between the axis of the scanning beam and the axis of the optic disc in the nasal-temporal direction (clockwise rotation around Y-axis) (Figure 2b1), the conical ppRPE/BM layer could be modified as follows:

$$\begin{pmatrix} x \\ y \\ z \end{pmatrix} = \begin{pmatrix} \cos(\beta) & 0 & \sin(\beta) \\ 0 & 1 & 0 \\ -\sin(\beta) & 0 & \cos(\beta) \end{pmatrix} * \begin{pmatrix} r * \cos(\alpha) \\ r * \sin(\alpha) \\ r * \tan(\gamma) \end{pmatrix}, \tag{2}$$

which could be also expressed as follows:

$$\begin{cases} x = r * [\cos(\alpha) * \cos(\beta) + \tan(\gamma) * \sin(\beta)] \\ y = r * \sin(\alpha) \\ z = r * [-\cos(\alpha) * \sin(\beta) + \tan(\gamma) * \cos(\beta)]. \end{cases} \tag{3}$$

Adding a tilt angle (θ) between the axis of the scanning beam and the axis of the optic disc in the nasal-temporal direction (clockwise rotation around X-axis) (Figure 2c1), the conical ppRPE/BM layer could be represented as follows:

$$\begin{pmatrix} x \\ y \\ z \end{pmatrix} = \begin{pmatrix} 1 & 0 & 0 \\ 0 & \cos(\theta) & \sin(\theta) \\ 0 & -\sin(\theta) & \cos(\theta) \end{pmatrix} * \begin{pmatrix} r * [\cos(\alpha) * \cos(\beta) + \tan(\gamma) * \sin(\beta)] \\ r * \sin(\alpha) \\ r * [-\cos(\alpha) * \sin(\beta) + \tan(\gamma) * \cos(\beta)], \end{pmatrix} \tag{4}$$

which could be also expressed as follows:

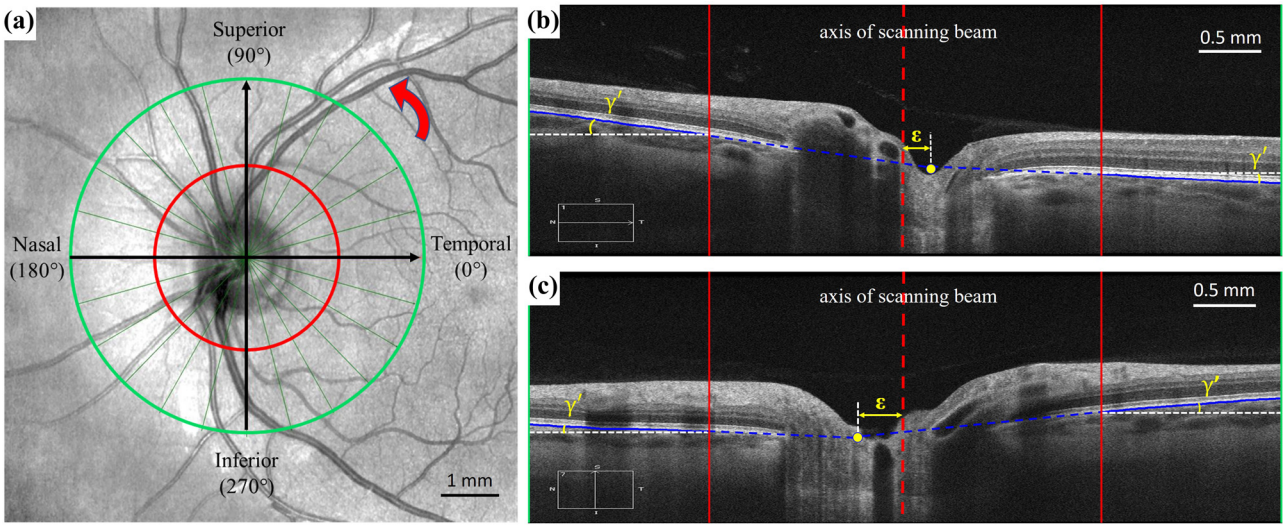

Figure 3: (a) Enface projection of the radial OCT centered over the optic disc. Twelve radial scans (green line) were acquired for each optic disc. The insert indicates the position of the corresponding scan shown in panel b (nasal-temporal direction) and panel c (superior-inferior direction). The red circle marks the inner boundary of the peripheral region of the optic disc for segmentation, and the green circle marks the outer boundary of the OCT scan. The radial position of the scan was assigned counterclockwise (marked with red circle arrow) starting from 0° at the temporal direction. (b) The ppRPE/BM layer angle (γ') and the eccentric distance (ε) in OCT scan at the nasal-temporal direction. (c) The ppRPE/BM layer angle (γ') and the eccentric distance (ε) in OCT scan at the superior-inferior direction. In panels b and c, the red line marks the inner boundary of the ppRPE/BM layer, and the green vertical boarder marks the outer boundary of the ppRPE/BM layer. The solid blue line highlights the portion of the ppRPE/BM layer analyzed in this study, and the dashed blue line marks the extension of the ppRPE/BM layer. The dashed red line indicates the axis of the scanning beam. The solid yellow dot is the intersection point of the two extended lines (dashed blue line) of the ppRPE/BM layer.

$$\begin{cases} x = r * [\cos(\alpha) * \cos(\beta) + \tan(\gamma) * \sin(\beta)] \\ y = r * \sin(\alpha) * \cos(\theta) + \sin(\theta) * r * \\ \quad [-\cos(\alpha) * \sin(\beta) + \tan(\gamma) * \cos(\beta)] \\ z = -r * \sin(\alpha) * \sin(\theta) + \cos(\theta) * r * \\ \quad [-\cos(\alpha) * \sin(\beta) + \tan(\gamma) * \cos(\beta)]. \end{cases} \quad (5)$$

Adding the translation of the conical vertex (C_x, C_y) in the X–Y plane (Figure 2d1), the conical ppRPE/BM layer could be derived as follows:

$$\begin{cases} x = r * [\cos(\alpha) * \cos(\beta) + \tan(\gamma) * \sin(\beta)] + C_x \\ y = r * \sin(\alpha) * \cos(\theta) \\ \quad + \sin(\theta) * r * [-\cos(\alpha) * \sin(\beta) \\ \quad + \tan(\gamma) * \cos(\beta)] + C_y \\ z = -r * \sin(\alpha) * \sin(\theta) \\ \quad + \cos(\theta) * r * [-\cos(\alpha) * \sin(\beta) \\ \quad + \tan(\gamma) * \cos(\beta)]. \end{cases} \quad (6)$$

The common clinical data are composed of radial scans at 24 half cross-sectional angle (also referred to as radial angle, denoted as α', ranging from 0° to 345° with a step increase of 15°, Figure 4). To derive the relationship between the ppRPE/BM layer angle (γ') and the radial angle of (α'), we focused on the peripheral region of the optic disc (the gray region in Figure 4b) to be consistent with our experimental measurements. Again, the inner boundary radius (r_0) was a constant of 1.56 mm and outer boundary radius (r_1) was a constant of 3 mm. The X–Y coordinates of the inner point (P_0) and outer point (P_1) of the ppRPE/BM layer at the radial angle of α' can be determined from Figure 4a as follows:

$$\begin{cases} P_{0x}(\alpha') = r_0 * \cos(\alpha') \\ P_{0y}(\alpha') = r_0 * \sin(\alpha'). \end{cases} \quad (7)$$

$$\begin{cases} P_{1x}(\alpha') = r_1 * \cos(\alpha') \\ P_{1y}(\alpha') = r_1 * \sin(\alpha'). \end{cases} \quad (8)$$

For (α', r_0) in the fundus view, the corresponding (α, r) at the conical ppRPE/BM surface can be calculated by substituting equation (7) to the first two equations in equation (6), as shown in equation (9). Then, the

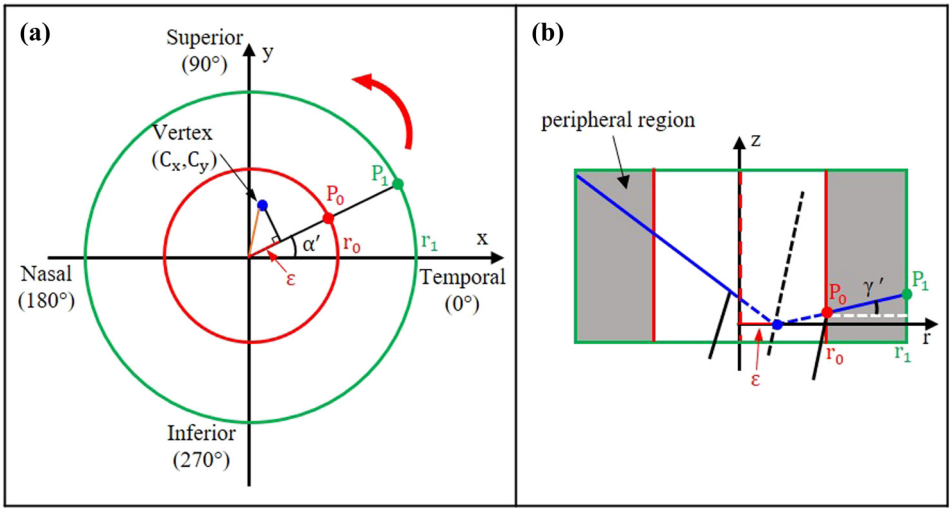

Figure 4: The fundus view (a) and a cross-sectional view (b) of the optic disc. (a) The red circle marked the inner boundary of the ppRPE/BM layer in the OCT scan, and the green circle marked the outer boundary. The distance of the surface vertex (C_x, C_y) to the origin of the X–Y coordinates (axis of scanning beam) was highlighted in orange. The eccentricity (ε) at the radial angle of α' was highlighted in red. (b) The cross-sectional view of the ppRPE/BM layer at a radial angle of α', and the peripheral region of the optic disc was highlighted in gray color. P_0 and P_1 are the inner point and outer point of the ppRPE/BM layer, respectively.

Z-coordinate $P_{0z}(\alpha')$ could be calculated by substituting the solved (α, r) to the third equation in equation (6). Similarly, for $P_{1z}(\alpha')$.

$$\begin{cases} x = r * [\cos(\alpha) * \cos(\beta) + \tan(\gamma) * \sin(\beta)] \\ \quad + C_x = r_0 * \cos(\alpha') \\ y = r * \sin(\alpha) * \cos(\theta) \\ \quad + \sin(\theta) * r * [-\cos(\alpha) * \sin(\beta) \\ \quad + \tan(\gamma) * \cos(\beta)] + C_y = r_0 * \sin(\alpha'). \end{cases} \quad (9)$$

Then, with Z-coordinates of P_0 and P_1, the ppRPE/BM layer angle (γ') at the radial angle of (α') could be calculated with equation:

$$\gamma'(\alpha') = \arctan\left(\frac{P_{1z}(\alpha') - P_{0z}(\alpha')}{r_1 - r_0}\right) * \frac{180}{\pi} (^\circ). \quad (10)$$

These equations (equations 6–10) have established the relationship among the clinical measurements in radial scans (γ' and α'), scanning tilt angles (β and θ), and the ppRPE/BM layer 3D angle (γ).

In addition, we can also calculate the eccentricity (ε) based on the projection of the vertex to the fundus view (Figure 4a) as follows:

$$E = \sqrt{(C_x^2 + C_y^2)} * \cos\left(\arctan\left(\frac{C_y}{C_x}\right) - \alpha'\right). \quad (11)$$

2.4 The control variate method for characterizing the ppRPE/BM layer angle variation

The measured ppRPE/BM layer angle (γ') variation across the radial directions was influenced by the ppRPE/BM layer 3D angle (γ), tilt angles (β & θ), and vertex translation (C_x, C_y), based on equations. The control variate method was adopted to quantify the impact of each aforementioned factor on the ppRPE/BM layer angle (γ') [27]. Specifically, we evaluated γ' with γ ranging from 0° to 10° with a step size of 2.5°, while keeping β as 5°, θ as 0°, and vertex parameters (C_x, C_y) as (0, 0). For all other cases, we set the control parameters: γ as 5°, β as 0°, θ as 0°, and vertex (C_x, C_y) as (0, 0). Then, we evaluated γ' with either β or θ ranging from 0° to 10° with a step size of 2.5°. The effect of vertex translation in the X–Y plane on the γ' variation was evaluated by varying C_x or C_y from −1.5 mm to 1.5 mm with a step size of 0.75 mm.

2.5 Reverse fitting for identifying the ppRPE/BM surface and its orientation

Given the clinical measurements of the ppRPE/BM layer angle and eccentricity, we are able to obtain individualized

parameters (γ, β, θ, C_x, C_y) for each OCT scanning data through reverse fitting. First, we could obtain the vertex parameters (C_x, C_y) from equation (11), which demonstrated that the eccentricity was independent of other parameters γ, β, θ. The vertex parameters (C_x, C_y) were calculated by the least square fitting of the 12 pairs of imaging data (ε, α') using MATLAB (MathWorks, version R2018a, USA).

Then, the remaining parameters (*e.g.*, γ, β, θ) could be obtained by minimizing the following objective function:

$$\mathrm{Diff}(\gamma, \beta, \theta) = \sum_{\alpha'=0}^{\alpha'=345} [\gamma'_{\exp}\alpha') - \gamma'_{\mathrm{mod}}(\alpha')]^2, \qquad (12)$$

where the subscript exp indicates the data measured from OCT images and subscript mod indicates the data calculated from our model – equation (10). For the ppRPE/BM layer angle (γ'), there were 24 data points corresponding to 24 half radial scans with radial angle (α') ranging from 0° to 345° with a step size of 15°. The unknown parameters are subjected to:

$$\begin{cases} 0° \le \gamma \le 10° \\ 0° \le \beta \le 10° \\ -10° \le \theta \le 10°. \end{cases} \qquad (13)$$

The boundary conditions of γ and β were based on our experimental observations and the documented radial scans, which normally had a positive tilt angle but rarely greater than 10° [21]. The boundary conditions of θ were based on our experimental observations that the tilt angle difference in the superior-inferior direction was within the range of –10° and 10°.

The optimal solution of equation (12) was obtained using the *fmincon* function of the MultiStart procedure in MATLAB [28]. To accelerate the computing speed, a parallel computing toolbox using multiple cores (n = 8) was applied. To ensure the fitted results were independent of the start points number in the MultiStart procedure, a convergence study was performed considering both the accuracy and efficiency. For example, we first ran the reverse fitting by using 1,000 starting points and then followed by another reverse fitting using 5,000 starting points. The results would be regarded as converged if the fitted ppRPE/BM layer parameters between the two simulations had a difference of less than 5%. If the difference was greater than 5%, we would add another 5,000 starting points and rerun the fitting until the differences between the consecutive simulations satisfy the 5% criterion. Based on the converged ppRPE/BM layer parameters (γ, β, θ, C_x, C_y), we then calculated the corresponding ppRPE/BM layer angle and eccentricity. The R^2 was then calculated to quantify the goodness of the reverse fitting.

3 Results

3.1 The ppRPE/BM layer angle variation model

Based on our mathematical model, the 2D cross-sectional view of the ppRPE/BM conical surface depend on four factors: the ppRPE/BM layer 3D angle (γ), the tilt angle (β) between the axis of the OCT scanning beam and the axis of the optic disc in the nasal-temporal direction, the tilt angle (θ) between the axis of the OCT scanning beam and the axis of the optic disc in the superior-inferior direction, and the location of the ppRPE/BM layer vertex to the axis of the scanning beam (C_x, C_y).

Figure 5 shows the role of the ppRPE/BM layer 3D angle γ and tilt angles (β and θ) on the measured ppRPE/BM layer angle γ' in various radial scans. The

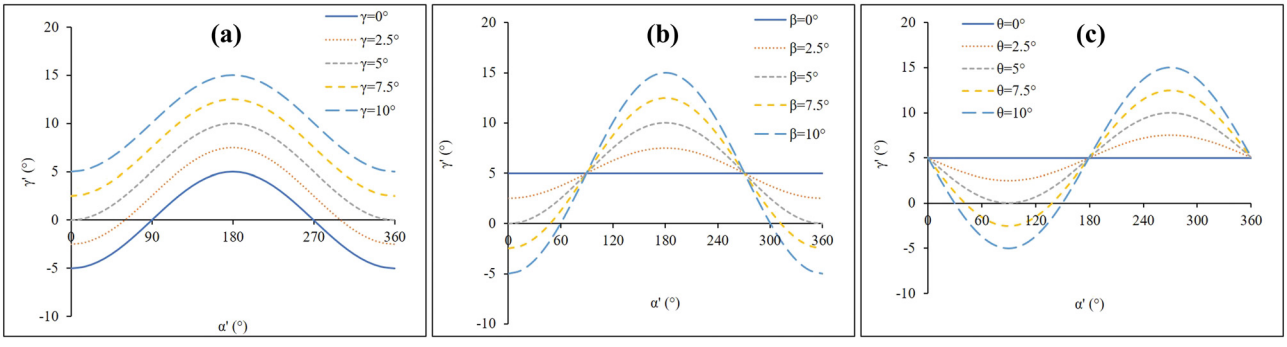

Figure 5: The ppRPE/BM layer angle γ' variation across the radial directions was influenced by (a) the ppRPE/BM layer 3D angle γ (constant β = 5°), (b) the tilt angle β (constant γ = 5°), and (c) the tilt angle θ (constant γ = 5°). The remaining parameters are zero.

ppRPE/BM layer angle γ' variation curve across radial directions exhibited the same amplitude regardless of the magnitude of the ppRPE/BM layer 3D angle γ. However, a larger γ induced an upward shift of the γ' variation curve as shown in Figure 5a. It is clear, in Figure 5b and c, that γ' across the radial directions exhibited the shape of the cosine-like curve with a nonzero β and the shape of sine-like curve with a nonzero θ. The amplitude of the cosine-like and sine-like curves increased with a larger tilt angle. As both tilt angles (β and θ) equal to zero, the measured ppRPE/BM layer angles γ' across all radial directions are equal to the ppRPE/BM layer 3D angle γ, shown as a straight line across all radial directions. It is worth noting that β induced the valley/peak ppRPE/BM layer angle γ' in the nasal-temporal direction (*e.g.*, 0° and 180°), while θ induced the valley/peak ones in the superior-inferior direction (*e.g.*, 90° and 270°).

Figure 6 has illustrated the role of the ppRPE/BM surface vertex translation (C_x, C_y) on the measured ppRPE/BM layer angle γ'. When the vertex was in the central region of the optic disc within a radius of 0.75 mm of the scanning center, the vertex translation has a minimal impact on the ppRPE/BM layer angle variation. When the vertex was closed to the boundary of the optic disc (*e.g.*, ±1.5 mm), the variation of the ppRPE/BM layer angle was slightly enlarged.

3.2 Reverse fitting for determining the ppRPE/BM layer 3D parameters

For each eye, we could measure eccentricity, γ' and α' at all radial scans, which was used for estimating the 3D ppRPE/BM morphology (γ, β, θ, C_x, C_y) based on our mathematical model. First, we use the method of least square to find the best fit for 12 measured eccentricity along 12 radial directions, which was used to determine the vertex parameters (C_x, C_y) in equation (11), which showed that the eccentricity is independent of the other parameters (γ, β, θ). Then, we are able to find the best fit for 24 measured γ' along 24 half radial directions, which was used to obtain parameters (γ, β, θ) from equation (10) through reverse fitting. The aforementioned two reverse fitting and the resulted ppRPE/BM morphology parameters (γ, β, θ, C_x, C_y) are shown in Figure 7 for the right eyes (n = 3) and Figure 8 for the left eyes (n = 3), respectively. It is clear that the calculated ppRPE/BM layer angle γ ranged from 3.9° to 5.5°, tilt angle β was from 2.7° to 6.0°, and θ was from −4.4° to 0.7°. It was observed that the variations of the ppRPE/BM layer angle across the radial directions were much like cosine curve. This is expected as the optic nerve head is naturally located at the nasal side of the eyeball (*e.g.*, tilt in nasal-temporal direction).

The goodness of fit of our model to the measured data points was quantified by the coefficient of determination (R^2). Values of R^2 are larger than 0.9 in most model predictions, indicating the effectiveness of the mathematical model developed in this study, which further illustrated the relationship between the ppRPE/BM 3D morphology and its 2D cross-sectional radial scans (commonly used in clinical practices).

The convergence study using the MultiStart procedure is illustrated in Table 1. It is clear that the ppRPE/BM layer parameters were converged with a larger number of the start points (N), but in the cost of a longer computation time.

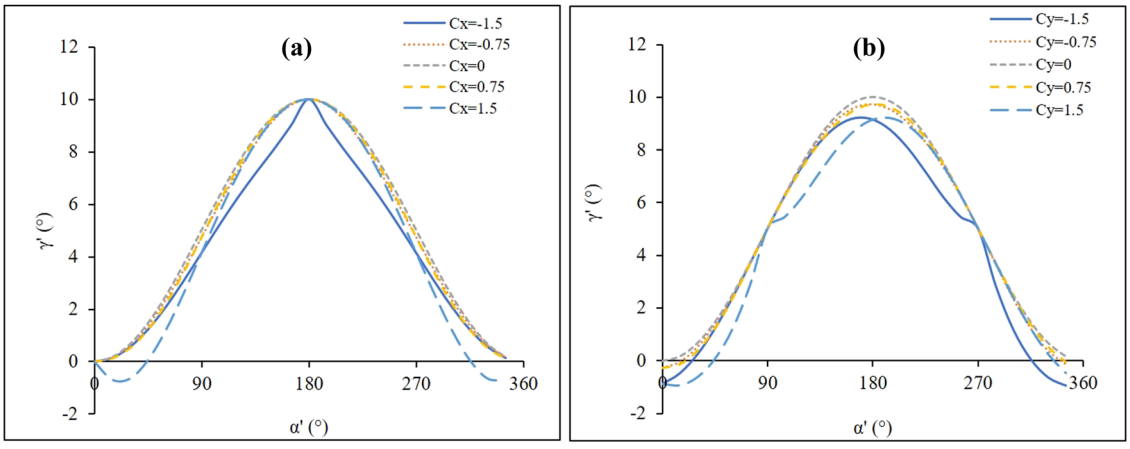

Figure 6: The influence of (a) the vertex translation of the ppRPE/BM surface in *X*-axis (C_x) and (b) the vertex translation of the ppRPE/BM surface in *Y*-axis (C_y) on the ppRPE/BM layer angle γ' variation across the radial directions, with γ = 5°, β = 0°, and θ = 0°.

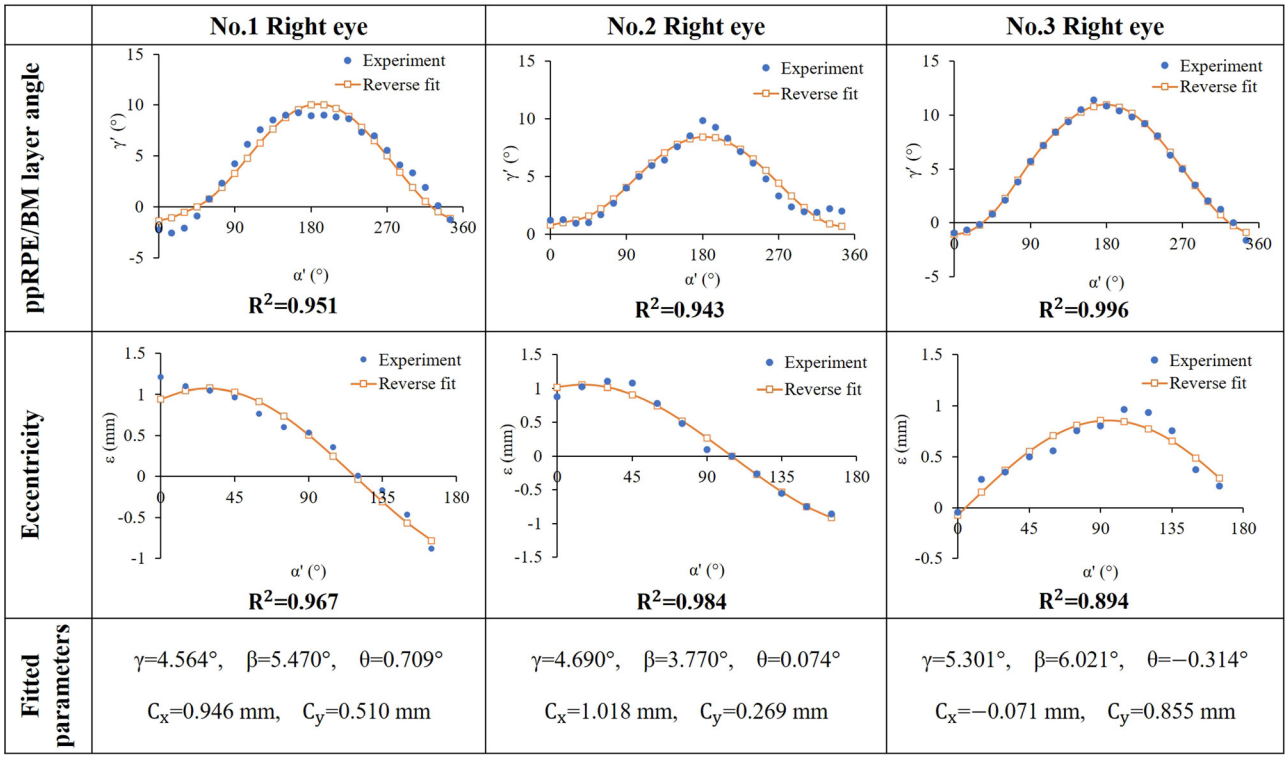

Figure 7: Comparison between the experimental measurements and model fitting results of with respect to γ' (first row) and ε (second row) of three right eyes. The fitted parameters were listed in the third row.

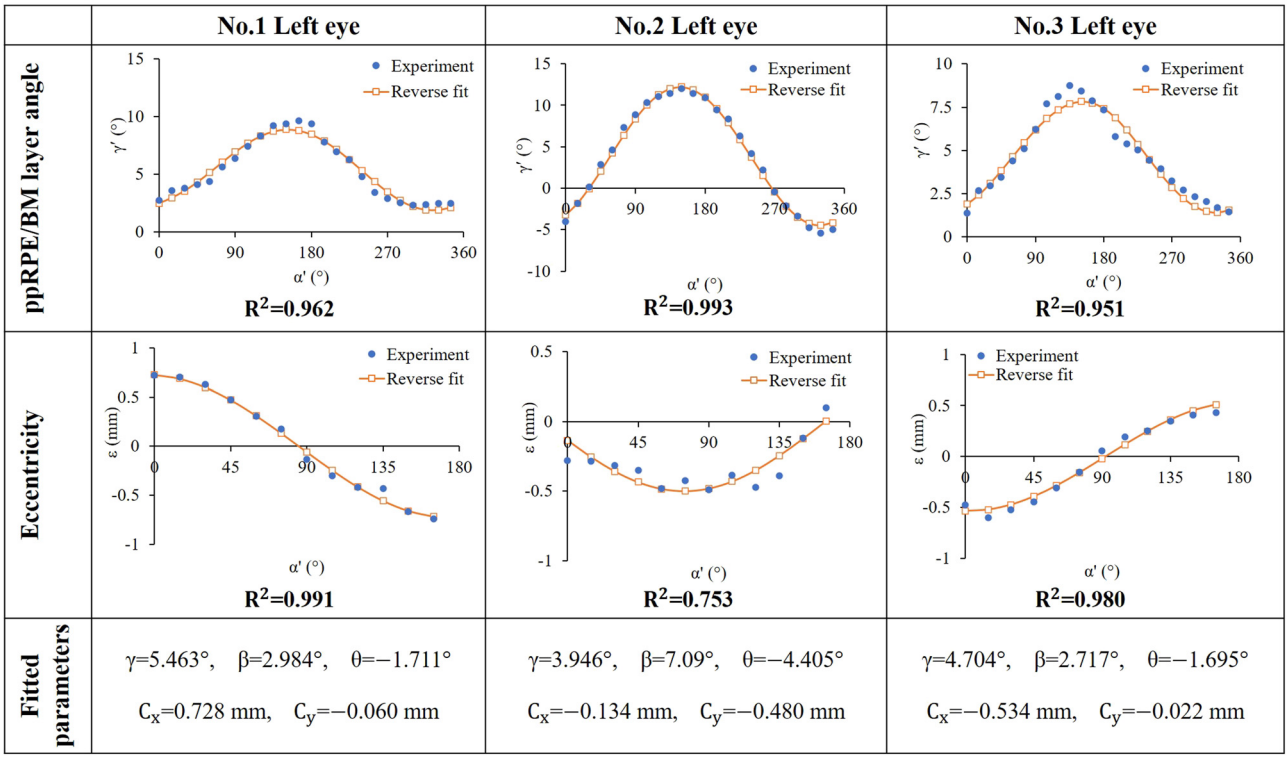

Figure 8: Comparison between the experimental measurements and model fitting results with respect to γ' (first row) and ε (second row) of three left eyes. The fitted parameters were shown in the third row.

Table 1: Convergence of the fitted ppRPE/BM layer parameters using MultiStart procedure (representative data: No. 1 right eye)

Number of start points (N)	Fitted ppRPE/BM layer parameters						Computing time (s)
	γ		β		θ		
	Value (°)	Change (%)	Value (°)	Change (%)	Value (°)	Change (%)	
1,000	4.439		5.506		0.499		839
5,000	4.597	3.56	5.510	0.07	0.618	23.85	3385
10,000	4.549	−1.04	5.512	0.04	0.684	10.68	6607
15,000	4.564	0.33	5.470	−0.76	0.709	3.65	9627

4 Discussion

In this study, a mathematical model has been developed to delineate the relationship between the ppRPE/BM layer 3D morphology and its 2D cross-sections in various radial directions. It has been found out that the measured ppRPE/BM layer angle variation across the radial directions depends on the ppRPE/BM layer 3D angle and the scanning tilt angles, which could be calculated by reverse fitting the measured 2D data points in the radial OCT scans. This study provided a mechanistic understanding of the ppRPE/BM layer 3D morphology, which could be further exploited for the diagnosis and prevention of the ocular and neurological diseases [29,30]. Moreover, the computational framework could be applied to other biomedical studies that integrate different 2D observations into 3D representation [31–33].

The impact of the ppRPE/BM layer 3D angle and scanning tilt angles on the measured ppRPE/BM layer angle in radial scans was evaluated using the control variate method. The tilt angle (β) between the axis of the OCT scanning beam and the axis of the optic disc in the nasal-temporal direction could be adjusted by moving the scanning beam horizontally (X-axis in Figure 1). The tilt angle (θ) between the axis of the OCT scanning beam and the axis of the optic disc in the superior-inferior direction could be adjusted by moving the scanning beam vertically (Y-axis in Figure 1). The relative position between the vertex of the ppRPE/BM layer and the axis of the scanning beam could be adjusted by moving the scanning center either horizontally or vertically. If the axis of the OCT scanning beam aligned with the axis of the optic disc, *e.g.*, no tilting, the measured ppRPE/BM layer angle will be the same across all radial directions (Figure 5b and c). However, the optic nerve head is naturally located at the nasal side of the eyeball (*e.g.*, tilt in nasal-temporal direction), which led to common image tilting during OCT scanning. To enforce a nontilt ppRPE/BM layer, the OCT scanning beam should be positioned towards the temporal portion of the pupil [13]. Thus, the measured ppRPE/BM layer angle variations along the different radial directions exhibited as cosine-like curve, as illustrated in our OCT image postprocessing (Figures 7 and 8). Our model revealed that ppRPE/BM layer angle variations were highly dependent on the ppRPE/BM layer 3D angle (Figure 5a) and the tilt angle between the axis of the OCT scanning beam and the axis of the optic disc (Figure 5b and c). Specifically, the midline of the angle variation curve depends on the ppRPE/BM layer 3D angle, and the amplitude of the angle variation curve depends on the tilt angles. Conversely, the position of the ppRPE/BM surface vertex has a minimal impact on the measured ppRPE/BM layer angle when the vertex is within the central region of the optic disc. The good match between the fitted curve and the clinical measurements from OCT image ($R^2 > 0.9$ in most cases) supported the aforementioned understandings and especially indicated the capability of the mathematical model in relating the variation of the ppRPE/BM layer angle along different radial directions with its 3D parameters.

The measured ppRPE/BM layer angle in radial scans was further reverse fitted into its 3D morphology in terms of the ppRPE/BM layer 3D angle. The quantified ppRPE/BM layer 3D angle was a comprehensive description of the peripapillary geometry, compared to the single measurement from a 2D cross-sectional scan [13,14]. The ppRPE/BM layer 3D angle could be considered as a new biomarker for evaluating the severity of the disease (*e.g.*, papilledema or idiopathic hypertension) and the effect of treatment [13,34]. Besides, it can avoid the tilt artifact that was born with the shape analysis of 2D scans [13]. Generally, the OCT scanning beam was required to be perpendicularly oriented over the optic nerve so as to obtain the symmetrical and untilted 2D scans. There is no need to do so by using the model developed in this study, as the reverse fitting will determine the ppRPE/BM layer 3D morphology parameters. In addition, the quantified ppRPE/BM layer 3D angle could also be used for the noninvasive ICP estimation since the ppRPE/BM layer

angle in 2D radial scans was found to change in response to the ICP level [13,14,19]. Moreover, such biomarker shows a promising prospect for accurate noninvasive ICP assessment as our previous study has shown that the minimum detectable change of the ppRPE/BM layer angle can be as low as 0.19° [6]. This could be particularly important when invasive ICP monitoring is not applicable due to ethical or safety concerns or difficulty in manipulating the test, such as for patients with normal-tension glaucoma [35] or acute mountain sickness [36–38], or for astronauts in the spaceflight [12,39].

We could automatically adjust the retinal OCT radial scans to eliminate the tilting effect based on the mathematical model developed in this study. It could then increase the accuracy and reproducibility of the retinal nerve fiber layer (RNFL) thickness in the optic nerve head or macula [15,16,20–23]. Hong *et al.* reported that different scan angles could induce significant artifact (*e.g.*, mean difference 13.26 ± 14.95 μm) in the measurement of RNFL thickness where the adjustment is necessary [16]. Lee *et al.* observed that the RNFL thickness measured in radial scans with the adjusted ppRPE/BM layer angle showed better reproducibility [23]. Furthermore, it was observed that the peripapillary RNFL thickness was significantly associated with the tilt degree of the optic disc, and a larger temporally tilted optic disc led to a thicker temporal RNFL [22,40]. Considering the association between myopia and optic disc tilt [41,42], the developed model might be transformed to the myopic population [40,43].

In this study, the ppRPE/BM layer 3D morphology was assumed as a perfect conical shape for developing the mathematical model that derives the ppRPE/BM layer angle in 2D radial scans under different imaging scenarios. Such an assumption was made to understand the association between 3D morphology and 2D radial scans. The application of this study is limited to the straight ppRPE/BM layer. The patients with curved ppRPE/BM layers (two out of 36 eyes) in our previous lumbar puncture study [6] will not be included.

In conclusion, the developed mathematical model in this study delineated how the ppRPE/BM layer angle across radial scans are related to the ppRPE/BM 3D parameters during the scanning process. The variations of the ppRPE/BM layer angle in different radial scans depend on the 3D angle and tilt angles. The ppRPE/BM layer 3D angle could be reversely fitted using the measured ppRPE/BM layer angles across radial directions. The ppRPE/BM layer 3D angle, first proposed herein, could be used to enhance the understanding of 2D radial scans and to exploit its potential as biomarkers of ocular diseases. In addition, the framework of this study could be transformed across many different biomedical studies that will require the integration of multifaceted observations in its broadest sense [44].

Funding information: The authors state no funding involved.

Author contributions: All authors have accepted responsibility for the entire content of this manuscript and approved its submission.

Conflict of interest: The authors state no conflict of interest.

References

[1] Fujimoto J, Swanson E. The development, commercialization, and impact of optical coherence tomography. Investig Ophthalmol Vis Sci. 2016;57(9):OCT1–13.
[2] Baghaie A, Yu Z, D'Souza RM. State-of-the-art in retinal optical coherence tomography image analysis. Quant Imaging Med Surg. 2015;5(4):603–17.
[3] Dong ZM, Wollstein G, Schuman JS. Clinical utility of optical coherence tomography in glaucoma. Investig Ophthalmol Vis Sci. 2016;57(9):OCT556–67.
[4] Kansal V, Armstrong JJ, Pintwala R, Hutnik C. Optical coherence tomography for glaucoma diagnosis: an evidence based meta-analysis. PLoS One. 2018;13(1):e0190621.
[5] Lee CS, Tyring AJ, Deruyter NP, Wu Y, Rokem A, Lee AY. Deep-learning based, automated segmentation of macular edema in optical coherence tomography. Biomed Opt Express. 2017;8(7):3440–8.
[6] Tong J, Dong P, Kedar S, Ghate D, Gu L. Three-dimensional characterization of peripapillary retinal pigment epithelium-basement membrane layer in patients following lumbar puncture. Appl Sci. 2020;10(5):1559.
[7] Zhang X, Medow JE, Iskandar BJ, Wang F, Shokoueinejad M, Koueik J, et al. Invasive and noninvasive means of measuring intracranial pressure: a review. Physiol Meas. 2017;38(8):R143.
[8] Hua Y, Tong J, Ghate D, Kedar S, Gu L. Intracranial pressure influences the behavior of the optic nerve head. J Biomech Eng. 2017;139:3.
[9] Cardim D, Robba C, Donnelly J, Bohdanowicz M, Schmidt B, Damian M, et al. Prospective study on noninvasive assessment of intracranial pressure in traumatic brain-injured patients: comparison of four methods. J Neurotrauma. 2016;33(8):792–802.
[10] Ghate D, Kedar S, Havens S, Fan S, Thorell W, Nelson C, et al. The effects of acute intracranial pressure changes on the episcleral venous pressure, retinal vein diameter and intraocular pressure in a pig model. Curr Eye Res. 2020;46:1–8.
[11] Marshall-Bowman K, Barratt MR, Gibson CR. Ophthalmic changes and increased intracranial pressure associated with

long duration spaceflight: an emerging understanding. Acta Astron. 2013;87:77–87.
[12] Zhang L-F, Hargens AR. Spaceflight-induced intracranial hypertension and visual impairment: pathophysiology and countermeasures. Physiol Rev. 2018;98(1):59–87.
[13] Sibony P, Kupersmith MJ, Rohlf FJ. Shape analysis of the peripapillary RPE layer in papilledema and ischemic optic neuropathy. Investig Ophthalmol Vis Sci. 2011;52(11):7987–95.
[14] Gampa A, Vangipuram G, Shirazi Z, Moss HE. Quantitative association between peripapillary Bruch's membrane shape and intracranial pressure. Investig Ophthalmol Vis Sci. 2017;58(5):2739–45.
[15] Hariri A, Lee SY, Ruiz-Garcia H, Nittala MG, Heussen FM, Sadda SR. Effect of angle of incidence on macular thickness and volume measurements obtained by spectral-domain optical coherence tomography. Investig Ophthalmol Vis Sci. 2012;53(9):5287–91.
[16] Hong S, Kim CY, Seong GJ. Adjusted peripapillary retinal nerve fiber layer thickness measurements based on the optic nerve head scan angle. Investig Ophthalmol Vis Sci. 2010;51(8):4067–74.
[17] Fan YY, Jonas JB, Wang YX, Chen CX, Wei WB. Horizontal and vertical optic disc rotation. The Beijing eye study. PLoS One. 2017;12(5):e0175749.
[18] Kraus MF, Liu JJ, Schottenhamml J, Chen C-L, Budai A, Branchini L, et al. Quantitative 3D-OCT motion correction with tilt and illumination correction, robust similarity measure and regularization. Biomed Opt Express. 2014;5(8):2591–613.
[19] Malhotra K, Patel MD, Shirazi Z, Moss HE. Association between peripapillary bruch's membrane shape and intracranial pressure: effect of image acquisition pattern and image analysis method, a preliminary study. Front Neurol. 2018;9:1137.
[20] Alonso-Caneiro D, Read SA, Vincent SJ, Collins MJ, Wojtkowski M. Tissue thickness calculation in ocular optical coherence tomography. Biomed Opt Express. 2016;7(2):629–45.
[21] Antony BJ, Stetson PF, Abramoff MD, Lee K, Colijn JM, Buitendijk GH, et al. Characterizing the impact of off-axis scan acquisition on the reproducibility of total retinal thickness measurements in SDOCT volumes. Transl Vis Sci Technol. 2015;4(4):3.
[22] Uji A, Abdelfattah NS, Boyer DS, Balasubramanian S, Lei J, Sadda SR. Variability of retinal thickness measurements in tilted or stretched optical coherence tomography images. Transl Vis Sci Technol. 2017;6(2):1.
[23] Lee K, Sonka M, Kwon YH, Garvin MK, Abramoff MD. Adjustment of the retinal angle in SD-OCT of glaucomatous eyes provides better intervisit reproducibility of peripapillary RNFL thickness. Investig Ophthalmol Vis Sci. 2013;54(7):4808–12.
[24] Medeiros FA, Zangwill LM, Bowd C, Vessani RM, Susanna Jr R, Weinreb RN. Evaluation of retinal nerve fiber layer, optic nerve head, and macular thickness measurements for glaucoma detection using optical coherence tomography. Am J Ophthalmol. 2005;139(1):44–55.
[25] Meditec CZ. Cirrus HD-OCT user manual. Dublin, CA, USA: Carl Zeiss Meditec; 2016.
[26] Mayer MA, Hornegger J, Mardin CY, Tornow RP. Retinal nerve fiber layer segmentation on FD-OCT scans of normal subjects and glaucoma patients. Biomed Opt Express. 2010;1(5):1358–83.
[27] Kucherenko S, Delpuech B, Iooss B, Tarantola S. Application of the control variate technique to estimation of total sensitivity indices. Reliab Eng Syst Saf. 2015;134:251–9.
[28] Moles CG, Mendes P, Banga JR. Parameter estimation in biochemical pathways: a comparison of global optimization methods. Genome Res. 2003;13(11):2467–74.
[29] Tong J, Kedar S, Ghate D, Gu L. Indirect traumatic optic neuropathy induced by primary blast: a fluid–structure interaction study. J Biomech Eng. 2019;141(10):101011.
[30] Tong J, Ghate D, Kedar S, Gu L. Relative contributions of intracranial pressure and intraocular pressure on lamina cribrosa behavior. J Ophthalmol. 2019;2019(3064949):3064949.
[31] Mozafari H, Zhou C, Gu L. Mechanical contribution of vascular smooth muscle cells in the tunica media of artery. Nanotechnol Rev. 2019;8(1):50–60.
[32] Lin S, Dong P, Zhou C, Dallan LAP, Zimin VN, Pereira G, et al. Degradation modeling of poly-l-lactide acid (PLLA) bioresorbable vascular scaffold within a coronary artery. Nanotechnol Rev. 2020;9(1):1217–26.
[33] Xing F, Zhou C, Hui D, Du C, Wu L, Wang L, et al. Hyaluronic acid as a bioactive component for bone tissue regeneration: fabrication, modification, properties, and biological functions. Nanotechnol Rev. 2020;9(1):1059–79.
[34] Sibony P, Kupersmith MJ, Honkanen R, Rohlf FJ, Torab-Parhiz A. Effects of lowering cerebrospinal fluid pressure on the shape of the peripapillary retina in intracranial hypertension. Investig Ophthalmol Vis Sci. 2014;55(12):8223–31.
[35] Baneke AJ, Aubry J, Viswanathan AC, Plant GT. The role of intracranial pressure in glaucoma and therapeutic implications. Eye. 2020;34(1):178–91.
[36] Keyes LE, Paterson R, Boatright D, Browne V, Leadbetter G, Hackett P. Optic nerve sheath diameter and acute mountain sickness. Wilderness Environ Med. 2013;24(2):105–11.
[37] DiPasquale DM, Muza SR, Gunn AM, Li Z, Zhang Q, Harris NS, et al. Evidence for cerebral edema, cerebral perfusion, and intracranial pressure elevations in acute mountain sickness. Brain Behav. 2016;6(3):e00437.
[38] Tian X, Zhang B, Jia Y, Wang C, Li Q. Retinal changes following rapid ascent to a high-altitude environment. Eye. 2018;32(2):370–4.
[39] Vijay V, Mollan SP, Mitchell JL, Bilton E, Alimajstorovic Z, Markey KA, et al. Using optical coherence tomography as a surrogate of measurements of intracranial pressure in idiopathic intracranial hypertension. JAMA Ophthalmol. 2020;138(12):1264–71.
[40] Hwang YH, Yoo C, Kim YY. Myopic optic disc tilt and the characteristics of peripapillary retinal nerve fiber layer thickness measured by spectral-domain optical coherence tomography. J Glaucoma. 2012;21(4):260–5.
[41] How AC, Tan GS, Chan Y-H, Wong TT, Seah SK, Foster PJ, et al. Population prevalence of tilted and torted optic discs among an adult Chinese population in Singapore: the Tanjong pagar study. Arch Ophthalmol. 2009;127(7):894–9.
[42] You Q, Xu L, Jonas J. Tilted optic discs: the Beijing eye study. Eye. 2008;22(5):728–9.
[43] Shin H-Y, Park H-YL, Park CK. The effect of myopic optic disc tilt on measurement of spectral-domain optical coherence tomography parameters. Br J Ophthalmol. 2015;99(1):69–74.
[44] Mozafari H, Wang L, Lei Y, Gu L. Multi-scale modeling of the lamellar unit of arterial media. Nanotechnol Rev. 2019;8(1):539–47.